Chicardi, E.; García-Garrido, C.; Sayagués, M.; Torres, Y.; Amigó, V.; Aguilar, C. (01-2). Development of a novel fcc structure for an amorphous-nanocrystalline Ti-33Nb-4Mn (at.%) ternary alloy. Materials Characterization. 135:46-56. https://doi.org/10.1016/j.matchar.2017.11.021

Development of a novel fcc structure for an amorphous-nanocrystalline Ti-33Nb-4Mn (at. %) ternary alloy

E. Chicardi[1*], C. García-Garrido[2], M.J. Sayagués[2], Y. Torres[3], V. Amigó[4] and C. Aguilar[1]

[1] Department of Metallurgical Engineering and Materials, Universidad Técnica Federico Santa María, Av. España 1680, Valparaíso, Chile.

[2] Instituto de Ciencia de Materiales de Sevilla (ICMSE-CSIC), Américo Vespucio 49, 41092 Sevilla, Spain.

[3] Department of Engineering and Materials Science and Transportation, University of Seville, Av. Camino de los Descubrimientos s/n, 41092 Seville, Spain

[4] Instituto de Tecnología de Materiales, Universitat Politècnica de València. Ciudad Politécnica de la Innovación, Carrer de l'Enginyer Fausto Elio, s/n, 46022 València, Spain.

Abstract.

In this work, a novel amorphous-nanocrystalline titanium-niobium-manganese solid solution ternary alloy with a Ti-33Nb-4Mn (at.%) nominal composition was developed by a High-Energy Mechanical Alloying. Nb and Mn were added to the elemental Ti as a β-phase (*bcc*) stabilizer and an amorphization promoter, respectively. The system evolved from the elemental Ti, Nb and Mn raw materials to a body centred cubic (*bcc*) TiNbMn alloy and, finally, to the formation of an original and stable face centred cubic (*fcc*) nanocrystalline TiNbMn alloy, not reported until now, at short milling time (20h). This alloy remains invariant until 120h. In turn, the partial amorphization of the system occurs and increases until at intermediate milling time (80h). The production

of both original *fcc* and the amorphous TiNbMn alloy may be beneficial for reducing the Young's modulus and improving the mechanical strength pursued for the Ti alloy. The optimal milling time respect to the amorphization, nanocrystalline size and Fe mount from milling media was 60 h and 80 h (**TiNbMn60h** and **TiNbMn80h**), with more than 50 wt.% of an amorphous phase and a crystalline domain size of approximately 5 nm.

*__Corresponding author__. Email address: ernesto.chicardi@usm.cl

Development of a novel fcc structure for an amorphous-nanocrystalline Ti-33Nb-4Mn (at. %) ternary alloy

Abstract.

In this work, a novel amorphous-nanocrystalline titanium-niobium-manganese solid solution ternary alloy with a Ti-33Nb-4Mn (at.%) nominal composition was developed by a High-Energy Mechanical Alloying. Nb and Mn were added to the elemental Ti as a β-phase (*bcc*) stabilizer and an amorphization promoter, respectively. The system evolved from the elemental Ti, Nb and Mn raw materials to a body centred cubic (*bcc*) TiNbMn alloy and, finally, to the formation of an original and stable face centred cubic (*fcc*) nanocrystalline TiNbMn alloy, not reported until now, at short milling time (20h). This alloy remains invariant until 120h. In turn, the partial amorphization of the system occurs and increases until at intermediate milling time (80h). The production of both original *fcc* and the amorphous TiNbMn alloy may be beneficial for reducing the Young's modulus and improving the mechanical strength pursued for the Ti alloy. The optimal milling time respect to the amorphization, nanocrystalline size and Fe mount from milling media was 60 h and 80 h (**TiNbMn60h** and **TiNbMn80h**), with more than 50 wt.% of an amorphous phase and a crystalline domain size of approximately 5 nm.

Keywords: Ti alloy; niobium; manganese; Amorphous; nanocrystalline; mechanical alloying.

1. INTRODUCTION.

Titanium and its alloys are important metallic materials used in a wide range of applications, such as the aerospace, aeronautic, automotive, chemical and biomedical industries [1-3], due to their interesting properties including high mechanical strength, lightweight, highest specific strength, excellent high temperature oxidation resistance and biocompatibility [4-6].

Related to biomaterials, both commercial pure Ti and its alloys are widely used in implants for bone tissue replacement. Concretely, the first generation of Ti alloys, referred as Ti6Al4V, with mainly hexagonal closely packed structure (*hcp*, α-phase), possess excellent mechanical strength but relatively poor wear resistance, lower hardness and higher stiffness than human bone tissues [7, 8]. The excessive difference between the Young's modulus (E) of Ti and the first generation Ti alloys (110-140 GPa) in comparison with the human bones (21–18 GPa for cortical and 15–10 GPa for trabecular bones [9, 10]) results in bone resorption and eventual loosening of the implants [11], known this problem as stress-shielding phenomenon [12]. In addition, Al and V, together with other elements (V, Ni, Co, Cr, Be, etc.) are toxic for the human body and/or cause allergic reactions [13, 14].

A second generation of Ti alloys, with non-toxic elements, such as Nb, Mo, Zr or Ta [12], were developed as a first attempt to solve the Young's modulus mismatch. In this case, they possess body centred cubic structure (*bcc*, β-phase) instead of the typical α-phase. This β-Ti alloys were fabricated searching their better mechanical properties than α-phase, mainly high fatigue resistance and low elastic modulus [15, 16], that make them more appropriated candidates as biomaterial for bone tissue replacement implants. However, although low E values (50-80 GPa) close to those of human bone can be achieved for some β-Ti alloys [17, 18], they present problems

associated with their mechanical performance and chemical stability due to their higher density, low creep strength, low tensile ductility in an aged state and low wear resistance [18].

For that reason, another recent way to solve the Young's modulus (E) mismatch involves the synthesis of porous Ti materials (foams) with different porosity arrangements [9, 19, 20]. For bone replacement purposes, foams are attractive due to facilitate the ingrowth of tissue and cells in the implants. However, in this case, the main disadvantage of metallic foams is the high volume porosity necessary that result in poor mechanical strength.

Again, new efforts are being directed towards developing new alloys and/or microstructures with improved mechanical properties to address the Young's modulus mismatch. In this sense, Ti alloys with nanocrystalline and/or amorphous phases are of great interest because they exhibit an unusual combination of properties including strength, ductility, high fracture toughness, and good corrosion resistance [21-23]. In contrast, coarse-grained materials lack these chemical and physical properties [24].

Related to the attention to form amorphous alloys, Mn has been reported as an element that promotes the amorphization [25-27]. Particularly, there it was reported how it is possible to reach a complete amorphization degree for the binary $Nb_{0.5}Mn_{0.5}$ and $Ti_{0.5}Mn_{0.5}$. A general requirement for amorphous phase formation is a significant difference in the atomic sizes between the constituent elements, which introduces a large strain into the alloy [26, 28]. Thus, the atomic radius of Ti, Nb and Mn are 0.176, 0.198 and 0.161 nm, respectively [29]. Besides, the Mn acts as a co-factor in bone mineralization as well as bone cartilage and collagen formation [30], that could be as an extra positive factor for using Mn as constituent of Ti based alloys biomaterials.

Powder Metallurgy (PM) process is an interesting approach to synthesize Ti alloys because this process allows the production of net-shaped components and materials with a broad spectrum of properties [31]. An interesting PM processing technique is High Energy Mechanical Alloying (HEMA), which allows for the production of Ti alloys with homogeneous compositions and special microstructures that are difficult to achieve by casting, forging and mechanical working processes [32]. HEMA is a non-equilibrium, simple and versatile process that transfers high energy from milling balls to the alloy powder during the milling process [33]. HEMA is a dry, solid-state powder processing technique that involves repeated welding, fracturing and re-welding of powder particles in a high-energy ball mill. The main attributes of HEMA include the extension of a solid solution, production of a fine dispersion of a secondary phase, synthesis of novel crystalline, quasi-crystalline and amorphous phases and structure refinement in the nanometre range [33, 34]. The two last characteristics are very interesting for the purpose of this work.

Therefore, taking into account all aspect abovementioned, this work was focused on the synthesis of an amorphous and/or nanocrystalline Ti-33Nb-4Mn (at.%) ternary alloy by HEMA using a high-energy planetary mill as potential raw materials for a new generation of Ti alloys for bone tissue replacement implants. Finally, it is necessary to comment that Nb was added to the alloy due to it is a non-toxic element for the human body, a β-phase stabilizer (preventing the undesirable α-phase (*hcp*) formation and the *stress-shielding* effect abovementioned) and it increases the mechanical strength, as reported Geetha et al. [12]. All these properties are important due to this alloy would be a potential material for bone replacement implant.

2. EXPERIMENTAL PROCEDURE.

A mixture of titanium metal powder (CAS number 7440-32-6, 99.6% purity, < 325 mesh, NOAH tech, San Antonio, TX, USA), niobium metal powder (CAS number 7440-03-1, 99.9% purity, < 325 mesh, NOAH tech.) and manganese metal powder (CAS number 7439-96-5, 99.9% purity, < 325 mesh, NOAH tech.) with a nominal composition of 63Ti-33Nb-4Mn (at.%) was milled.

Concretely, 20 g of the powder mixture was introduced with 95 balls (Ø=8 mm. and m=2.1g) in a 300 ml vial (both composed of tempered steel, 67HRC). They were mechanically alloyed in a planetary ball mill (PM400, Retsch) under an inert atmosphere (i.e., argon gas, $H_2O \leq 8$ ppm and $O_2 \leq 2$ ppm, Linde Group, Spain) and at spinning rate of 300 rpm for 1 h to 120 h. A ball-to-powder ratio (BPR) of 10 was employed. In addition, 3 wt. % of hexane (CAS number 110-54-3, 99% purity, NOAH tech.) was added to the powder mixture as a process control agent (PCA) to avoid welding of the transition metals to the balls and vial.

Then, the as-milled powder mixtures obtained after different milling times were collected under an Ar atmosphere in an inert box (850-NB Nitrogen Dry Box, Plas-Labs Inc.) and dispersed in hexane to prevent oxidation during handling.

The collected specimens were labelled based on their milling times (Table 1) from the specimen milled for only 1 h (**TiNbMn1h**) to the specimen milled for the longest milling time (**TiNbMn120h**).

To characterize the powder mixtures, X-ray diffraction (XRD) patterns were recorded using a PANalytical X'Pert Pro instrument equipped with a θ/θ goniometer, a Cu Kα radiation source (40 kV, 40 mA), a secondary Kb filter and an X'Celerator detector. The XRD patterns were obtained by scanning from 2θ between 20° and 150° in the step-scan mode with 0.02° steps and a counting time of 275 s/step. The space

group symmetry (SGS), lattice parameters, crystalline domain size (D), microstrain (e) and quantification of the nanocrystalline and amorphous phases were determined from the complete set of peaks in the XRD diagrams using the Fullprof Suite toolbar and Rietveld analysis, which include the Dicvol (used for powder diffraction indexing by the Dichotomy method), WinPLOTR and FullProf programs. The PDF-4+ database, which was obtained from the International Centre for Diffraction Data (ICDD), and the Crystallography Open Database (COD), were used for comparison and structural elucidation. Silicon powder (Standard Reference Material 640e, NIST) was used to correct the instrumental error of the diffractometer and calibrate the positions of the diffraction lines as an internal standard pattern for amorphous phase quantification by Rietveld analysis [35].

Scanning electron microscopy (SEM) images of the as-milled powder mixture were recorded on a Hitachi S-4800 field emission SEM instrument in secondary electron mode at an acceleration voltage of 5 kV. The Ti, Nb, Mn and Fe transition metals (Fe coming from the milling media) as well as the C and O content were measured by X-ray energy dispersive spectrometry (XEDS) using a detector coupled with SEM at an acceleration voltage of 20 kV. For each milling time specimen, around 30 punctual measurements were performed. In addition, XEDS-SEM mapping was performed under the same experimental conditions. SEM images at different magnifications (1kx, 2kx and 5kx) were recorded to evaluate the average and distribution particle sizes (d) using Image Analysis (IA) as implemented in Image-Pro Plus 6.2.

High-resolution transmission electron microscopy (HRTEM) images and selected area electron diffraction (SAED) patterns were obtained for powder specimens on an FEG HRTEM microscope that was obtained from the FEI Company, USA (model

TECNAI G2 F30 S-twin) with scanning-transmission capabilities (STEM). The experiments were conducted at 300 kV with 0.2 nm point resolution. The microscope was equipped with a high-angle annular dark field (HAADF) detector from Fischione Instruments, USA (0.16 nm point resolution), and an INBCA ZX-max 80 silicon drift detector (SDD) for energy-dispersive X-ray analysis (EDX). The micrograph analysis, lattice spacing, fast Fourier transform (FFT) and phase interpretation were performed with the Gatan Digital micrograph software (Gatan Inc., USA). The powder samples were dispersed in acetone, and droplets of the suspension were deposited onto a PELCO® pure carbon film grid.

Finally, differential scanning calorimetry (DSC) was employed to confirm the melting temperature of . The tests were carried out using a DSC- 822e (Metter Toledo) from 40 °C to 550 °C at a heating rate of 40 °C·min^{-1} with free cooling. Two consecutive cycles were performed for each specimen to clearly differentiate the corresponding crystallization peaks.

3. RESULTS AND DISCUSSION.

3.1. Determination of phases.

The X-ray diffraction (XRD) patterns obtained for the Ti-33Nb-4Mn (at.%) ternary alloy, milled for 1 h to 120 h, are shown in Fig. 1. After 1 h, **TiNbMn1h** only exhibited peaks corresponding to the elemental powders (i.e., Ti (hexagonal close-packing structure and P63/mmc SGS), Nb (cubic structure, and Im3m SGS) and Mn (cubic structure and I-43m SGS)) according to the reference patterns (i.e., 044-1292, 034-0370 and 032-0637, respectively) in the PDF-4+ database. No alloys were formed at this shortest milling time. The lattice parameters for Ti, Nb and Mn were determined by Rietveld refinement and are listed in Table 1.

The background, the lattice parameters, the scale, the shape of peaks (using a Thompson-Cox-Hastings pseudo-Voigt axial divergence asymmetry equation), the atoms positions, the strain/size and the zero displacements have been the main parameters refined in the Rietveld analysis.

It is important to note that the goodness-of-fit (χ^2) and the weighted profile R-factor (R_{wp}) for the Rietveld refinement of all specimens (from **TiNbMn1h** to **TiNbMn120h**) were approximately 2 and less than 10%, respectively, which confirms an optimal fitting.

No significant deviation from these lattice parameters, which correspond to the previously mentioned reference patterns (Table 1 for comparison) were observed, which confirms that no metal alloys were formed. However, when the milling time was increased to 10 h (**TiNbMn10h**), these peaks disappeared, suggesting complete alloying of the initial Ti, Nb and Mn metals to form substitutional alloys and/or intermetallic compounds. In addition, new peaks were observed in the corresponding XRD pattern (Fig. 1). These peaks were assigned to three different phases. First, an alloy with face-centred cubic (*fcc*) structure and Fm3m SGS (1534903 Nb reference pattern in the COD database). Another alloy with body-centred cubic (*bcc*) structure and Im3m SGS (034-037 Nb reference pattern in the PDF-4+ database). Finally, Fe with body-centred cubic structure and Im3m SGS (006-0696 reference pattern in the PDF-4+ database), which was extracted from the milling media during the milling process. The first two alloys are expected to be TiNb, TiMn and/or NbMn binary alloys or, otherwise, TiNbMn ternary alloys due to the total absence of Ti, Nb and Mn peaks. This last result was confirmed as described below. For that reason, we labelled both alloys as *bcc*-TiNbMn and *fcc*-TiNbMn throughout the work. It is important to note that no oxidized phases or

carbides were detected, suggesting minor O_2 and C contamination, from the possible air that may have remained in the Ar box and the PAC, respectively.

For the specimen milled for 20 h (**TiNbMn20h**), the XRD indicated that the system evolved to form the *fcc*-TiNbMn alloy and elemental Fe coming from milling media (Fig. 1). Both phases remained invariant without the appearance of any other phases as the milling time increased to 120 h. Therefore, this suggests the *fcc*-TiNbMn alloy formed is a stable alloy.

The lattice parameters determined for this *fcc*-TiNbMn alloy (Table 1) exhibited slight variations, suggesting a lack of important modifications of the alloy composition with the milling time. Therefore, this alloy is expected to be the same as the nominal composition used, which was confirm and is discussed below. Thus, the differences between **TiNbMn20h** and **TiNbMn120h** are related to the microstructure (i.e., homogenization, crystalline domain size, lattice strain and amorphization degree). In addition, the lattice parameter for the *bcc*-TiNbMn alloy, formed at 10 h of milling time, is shown in Table 1 (**TiNbMn20h**).

As shown in Fig. 1, a decrease in the peak intensity and an increase in the peak width were observed for the *fcc*-TiNbMn alloy from **TiNbMn20h** to **TiNbMn80h**, and a slightly inverted behaviour was observed for the alloys from **TiNbMn80h** to **TiNbMn120h**. These results may be due to effect of the milling time on “D”, “e" and the amorphization degree.

The crystalline domain size and microstrain of the *fcc*-TiNbMn alloy were extracted from the Rietveld analysis and are shown in Table 1. For comparison, the same microstructural parameters were obtained for Ti and Nb present in the **TiNbMn1h** specimen. The “D” and “e” for Mn could not determined due to the existence of a single peak with very low intensity.

These results are shown in Fig. 2 and Table 1. First, the D value for elemental Ti and Nb (54 and 43 nm, respectively) in the **TiNbMn1h** specimen was substantially reduced to 30 and 16.5 nm for the *bcc*-TiNbMn and the *fcc*-TiNbMn alloys, respectively, formed after 10 h of milling (**TiNbMn10h**). This decrease in "D" was accompanied by an important microstrain (e) increase due to plastic deformation and crystalline defects that were introduced by the milling. Between **TiNbMn10h** to **TiNbMn20h,** the decrease in D was accompanied by a decrease in "e". This opposite behaviour was due to the important decrease in D (6.6 nm for **TiNbMn20h**) that is now in the order of typical flaws in metals (i.e., dislocations). The energy supplied by the milling process along with the low D allowed for the facile movement and annihilation of dislocations.

Nanostructures are formed by the deformation that occurs in shear bands that are located in unstrained grains. The grain size (or crystalline size) decreases steadily, and the shear band coalesces as the milling time increases. The small angle boundaries are replaced by higher angle grain boundaries, which implies grain rotation that produces disclinations [36]. This behaviour is reflected by the absence of texture (preferred orientation) in the electron diffraction pattern, which also contributes to X-ray peak diffraction broadening. Therefore, dislocation-free nanocrystalline grains were formed. As the milling continues, the nanocrystalline grains reach a saturation value. Due to the difficulty of dislocation generation at the nanocrystalline size, the existing dislocations will rearrange, and some other existing dislocations are eliminated [33]. Then, the strain and dislocation density decrease. But the dislocation density is not measured.

From a milling time of 20 h (**TiNbMn20h**) to 120 h (**TiNbMn120h**), which corresponds to the formation of only the *fcc*-TiNbMn alloy in the specimens, the D value was nearly invariant with only a slight decrease from 6.6 nm to 4.8 nm. In

contrast, during this period of milling, two different behaviours were detect on the microstrain (e). From **TiNbMn20h** to **TiNbMn80h**, "e" decreased due to the previously mentioned dislocation annihilation effect (i.e., the low crystalline domain size (D) allowed for movement of the dislocations to the grain boundary, which added to the energy supplied by the milling process. However, from **TiNbMn80h** to **TiNbMn120h,** the opposite "e" behaviour was observed. In this case, another effect has a more important influence. Some authors have hypothesized that the grain boundaries in ultrafine-grained (UFG) materials, processed by severe plastic deformation (SPD), which occurs in mechanical alloying (MA) [37], are characterized by excess grain boundary energy and the presence of long-range elastic stresses [38]. Thus, the ultrafine-grained TiNbMn alloys obtained at this point produced the increase of grain boundary energy, reaching a higher "e" values with the milling time from 80 h to 120 h.

In addition, the presence of Mn in the ternary alloys along with the small crystalline domain size (D) may allow for partial amorphization, which is consistent with a previous study [39]. The amorphous phase percentage was quantified by replicating the Rietveld analysis using now Si as an internal pattern. The results are shown in Table 1, and an example of the determination for the **TiNbMn60h** specimen is shown in Fig. 3. The amorphous phase increased with the milling time to 80 h (**TiNbMn80h**), where a 53 wt. % TiNbMn amorphized alloy was obtained. This high amorphous percentage for the TiNbMn alloy obtained could be interesting due to it can be used as raw material to obtain bulk partial amorphous biomaterials via a Field Assisted Sintering Technique (FAST), such as Spark Plasma Sintering (SPS) [40], Electrical Resistance Sintering (ERS) [41] and/or Capacitor discharge sintering (CDS) [42] consolidation processes. This fact is in order to maintaining the amorphous and the nanocrystalline structure. Beyond the 80h of milling time, partial recrystallization of the

amorphized TiNbMn alloy occurred due to the high milling energy applied (see Table 1).

3.2. Microstructural characterization.

The SEM images that correspond to all the specimens (from **TiNbMn1h** to **TiNbMn120h**) are shown in Fig. 4. The particle size decreased when the milling time increased to 60 h (i.e., the **TiNbMn60h** specimen). For longer milling times, the particle sizes slightly increased to 120 h (i.e., **TiNbMn120h**). The main particle size reduction was produced during the first ten hours of milling from **TiNbMn1h** to **TiNbMn10h** (note that a lower magnification was used for the **TiNbMn1h** SEM micrograph shown in Fig. 4). In addition, evolution the particle morphology occurred, and spherically shaped particles were obtained at longer milling times (from **TiNbMn60h** to **TiNbMn120h**) rather than the faceted initial particles that were obtained at shorter milling times (from **TiNbMn1h** to **TiNbMn40h**). The particle size decrease as well as the spherically shaped particles that were obtained at longer milling times may be beneficial for a potential powder consolidation process.

To confirm the particle size results, the particle size distribution was determined using image analysis (Fig. 5). To gain additional insight, the average particle size (d_{av}) and 50 (d_{50}) and 90 (d_{90}) percentiles are also included in Fig. 5. The most important reduction in the particle size occurred on going from the raw materials (< 45 μm or 325 mesh, for Ti, Nb and Mn, according to the values supplied by the manufacturer) to those obtained after 10 h of milling (**TiNbMn10h**) when the alloy formation began. Then, the particle size distributions decreased progressively to a smaller particle size from **TiNbMn10h** to **TiNbMn40h**. However, between 40 h (**TiNbMn40h**) and 80 h (**TiNbMn80h**) of milling, the particle size decrease substantially, which is consistent the increased formation of the amorphous phase for milling times between 60 h and 80

h. From 80 h (**TiNbMn80h**) to 120 h (**TiNbMn120h**) of milling, the distribution of particle sizes increase slightly due to particle welding that resulted from the high milling energy.

The XEDS mapping for the **TiNbMn10h** and **TiNbMn60h** specimens (Figs. 6 and 7, respectively) indicated optimal homogenization and distribution of the three compositional transition metals in the alloys (i.e., Ti, Nb and Mn). Although these results may appear to be inconsistent with the XRD patterns shown in Fig. 1, they indicate that the *bcc*-TiNbMn (formed at lower milling time) and *fcc*-TiNbMn alloys have similar Ti, Nb and Mn compositions. The punctual XEDS carried out on more than 30 particles randomly selected for each specimens (Table 2) provided relative Ti, Nb and Mn weight compositions closed to the nominal values, Ti-33Nb-4Mn (at.%), with similar standard deviations for all specimens. These results confirmed the optimal homogenization of Ti, Nb and Mn even for a short milling time (see Table 2). This assertion is not valid for the specimen milled for 1 h (**TiNbMn1h**), where almost no homogenization occurred. This result was confirmed by the standard deviation reported in Table 2 and the XRD results (Fig. 1). At this point, it is necessary to highlight the *fcc* structure is an original structure not previously observed for Ti alloys. The ball milling has promoted this *bcc* to *fcc* allotropic transformation, analogous to a similar evolution transformation reported by elemental Nb [43].

However, in the same XEDS mappings (Figs. 6 and 7), some dots or zones were observed on the micrographs, and these areas correspond to unalloyed Fe, which comes the milling media. The presence of only unalloyed Fe could be explained attending to the Ti-Fe, Nb-Fe and Mn-Fe binary diagrams [44]. The solubility at room temperature in the two first ones are non-existent and only a partial solubility was found for the Mn-Fe system. Thus, due to these aspects and the progressive introduction of Fe with the

milling time, when the complete TiNbMn alloy was already formed, avoided the alloying of Fe and the formation of undesirable intermetallic compounds.

The at.% of Fe increased with the milling time and reached an important percentage, as shown in Table 2. This important Fe quantity could be reduced using another milling media or softer milling conditions. Anyway, although Fe is not a starting element for the expected TiNbMn ternary alloy, it cannot be consider as detrimental element due to Fe is also used for biomedical applications [45, 46].

It is important to note that both oxygen and carbon, which could come from exposure to air during specimen manipulation and the possible partial hexane detected by the XEDS, suggesting lower hexane decomposition (mostly evaporated during milling) and lower oxidation of specimens (thanks to use hexane also as dispersant). In the particular case of oxygen, high affinity of Ti for O_2 could result in a presence of small quantities of O_2, not detectable by XEDS. However, this aspect could not be detrimental, due to some authors have found beneficial effects of small O_2 addition on the stability of Ti alloys [47].

Differential scanning calorimetry (DSC) was carried out on the **TiNbMn60h** specimen to confirm the partial amorphization and estimate the recrystallization temperature (Fig. 8a). First, the presence of an important exothermic peak was observed at approximately 380°C (T_c in Fig. 8a). This peak disappeared in the second heating cycle, confirming the irreversible nature of the crystallization peak. It is necessary to emphasize that the crystallization peak obtained for amorphous materials obtained by milling is usually wider and less intense than the corresponding for bulk metallic glasses (BMGs) developed by quenching or cast form the melted alloy [48, 49]. This can be explain due to the partial amorphous material obtained by milling is formed by distortion of the lattice parameter for the nanocrystal material formed, i.e., can be

exceptionally exist a short-range order. As opposite, the BMGs are formed from melted alloy and not from a crystalline phase, without any short-range order.

In addition, the XRD pattern of the same **TiNbMn60h** specimen was recorded after DSC (Fig. 8b). The existing phases were similar before and after DSC, except for the disappearance of the small "hump" (marked with an ellipse in Fig. 8b) between the *fcc*-TiNbMn peaks, which confirmed the crystallization of the amorphous phase. In addition, additional peaks were observed in the DSC (Fig. 8a) at an intermediate temperature that corresponded to the glass transition temperature (T_g = 270°C, endothermic), typical peak for amorphous materials. Again, this peaks disappeared for the second heating cycle due to the alloys was crystallized during the first one. Finally, the small endothermic peak observed at 69ºC corresponded to the evaporation temperature of the hexane used as PCA and dispersant for the alloys.

To confirm the formation of the amorphous and nanocrystalline alloys that were detected by XRD and DSC, selected area electron diffraction (SAED) and high-resolution transmission electron microscopy (HRTEM) images were recorded for the **TiNbMn10h** and **TiNbMn60h** alloys (Fig. 9 for SAED and Fig. 10 for HRTEM). In addition, the FFT of the HRTEM images was obtained (insets in Fig. 10). The SAED that corresponded to a region of the **TiNbMn10h** alloy (inset of Fig. 9a), an electron diffraction pattern that primarily corresponded to a nanocrystalline phase was observed. Only an intense electron diffraction spot was detected, suggesting the presence of a residual microdomain size alloy. It is important to note that this study was carried out for a large number of specimen areas, and the same results were always obtained. By measuring the blurred diffraction circles, the **d**(*hkl*) spacing was indexed to the *bcc*-TiNbMn structure, and the (110) and (211) reflections of this phase were observed (depicted on the SAED). In addition, the intense electron diffraction spot was assigned

to the (110) reflection for Fe due to contamination from the milling media. In contrast, no electron diffraction rings were detected for the *fcc*-TiNbMn. This result confirms that this phase is not present in the analysed zones, which may be due to the lower *fcc*-TiNbMn percentage than the *bcc*-TiNbMn in the **TiNbMn10h** specimen.

The SAED analysis of the **TiNbMn60h** specimen reveals only diffuse scattering, and this feature indicates that the studied regions are primarily amorphous, as shown in the inset of Fig. 9b. In some regions, a very diffuse ring was observed, which was indexed as the (200) plane of the *fcc* alloy structure. No *bcc*-TiNbMn was obtained at this milling time, which is in good agreement with the XRD results. It is important to note that the same ring can be indexed to the (110) reflection of elemental Fe. However, in this case, the reflection is more diffuse than that for the **TiNbMn10h** specimen due to the increased milling time, indicating an important decrease in the crystalline domain size in the Fe phase.

Finally, attending to the HRTEM study, for the **TiNbMn10h** specimen (Fig. 10a), only nanodomains were observed along with small amorphous zones (marked as black squares) between the nanodomains. This result suggested the beginning of the specimen amorphization. The FFT corresponding to this area is shown in the inset of Fig. 10a, and two rings that correspond to (110) spacing of the *bcc*-TiNbMn phase and (200) plane corresponding to the *fcc*-TiNbMn were observed. Several nanocrystals with an average size of 8 nm were observed (marked as round areas), and the planar spacing was measured, indexed and marked on the micrograph. The nanocrystal nearly oriented along the [111] zone axis of a cubic structure was marked with a red square, and the measurement of reflections in the FFT (inset depicted) indicates that this small domain corresponds to the *bcc* TiNbMn phase of the alloy.

As shown in Fig. 10b for the **TiNbMn60h** specimen, the interplanar spacings were difficult to detect in the HR micrograph, and only a small nanocrystalline domain (white square) that corresponded to the (200) planar spacing of the *fcc*-TiNbMn was observed. The FFT of the image (inset) reveals primarily diffuse scattering, indicating the high amorphization of the specimen compared to the **TiNbMn10h** specimen. This result is consistent the XRD (Fig. 1) and SAED (Fig. 9b) results.

4. CONCLUSIONS.

1. A titanium-niobium-manganese ternary alloy with a nominal composition of Ti-33Nb-4Mn (at.%) was obtained using a high-energy mechanical alloying (HEMA) process.

2. The obtained alloy evolved from two nanocrystalline phases (*bcc* and *fcc* TiNbMn alloys) after a short milling time (i.e., 10 h) to an amorphous-nanocrystalline (*fcc*) alloy at an intermediate milling time. The amorphous percentage increased until a milling time of 80 h, and then slightly decreased until a milling time of 120 h.

3. The development of a new structure for Ti alloys, i.e., the *fcc*-TiNbMn alloy and an amorphous TiNbMn phase, in substitution of the hexagonal structure, *hcp*-Ti alloys, may be beneficial for reducing the Young's modulus and improving the mechanical strength of a future consolidated TiNbMn specimen via a FAST (Field Assisted Sintering Technique) process.

4. The optimal milling time with respect to the amorphization, nanocrystalline size and Fe percentage was 60 h and 80 h (**TiNbMn60h** and **TiNbMn80h**). These specimens contained more than 50 wt.% of an amorphous phase and a crystalline

domain size of approximately 5 nm. Both properties may be beneficial for the subsequent consolidation process.

5. The presence of Fe, coming from the milling media, increased with the milling time, but remains majority unalloyed in the as-milled material. The high Fe percentage indicates the need for studying the use of different milling media, such as ceramic materials (yttria-stabilized zirconia (YSZ) and alumina (Al_2O_3)) or, also, using softer milling conditions.

Acknowledgements.

This work was supported under postdoctoral grant No. 3150060, which is financed by the FONDECYT fund (Government of Chile).

FIGURE CAPTIONS.

Figure 1. X-ray powder diffraction patterns for the TiNbMn alloy milled for 1 h to 120 h. (■) *hcp*-Ti (P63/mmc Space Group Symmetry, SGS); (●) *bcc*-Nb (Im3m SGS); (▼) *bcc*-Mn (I-43m SGS); (O) *bcc*-TiNbMn alloy (Im3m SGS); (★) *fcc*-TiNbMn alloy (Fm3m SGS); (◆) *bcc*-Fe (Im3m SGS).

Figure 2. Crystalline domain size (D) and microstrain (e) of the TiNbMn alloy milled for 1 h to 120 h.

Figure 3. Rietveld refinement carried out on the XRD diagram with Si introduced as an internal pattern for the **TiNbMn60h** specimen. (★) *fcc*-TiNbMn alloy (Fm3m SGS); (◆) *bcc*-Fe (Im3m SGS); (⊙) Silicon used as internal pattern.

Figure 4. Scanning electron microscopy (SEM) images for the TiNbMn alloy milled for different time periods ranging from 1 h to 120 h. Note that the corresponding SEM

image for the specimen milled for 1 h (**TiNbMn1h**) is shown at lower magnification due to the larger particle size.

Figure 5. Particle size distribution for the TiNbMn alloy milled for different period of times ranging from 1 h to 120 h. The corresponding histogram for the **TiNbMn1h** alloy is presented at a different scale due to the larger particle size. d_{av}: Average particle size; d_{50}: 50th percentile; d_{90}: 90th percentile.

Figure 6. Characteristic compositional XEDS-SEM mapping for the **TiNbMn10h** alloy after 10 h of milling time.

Figure 7. Characteristic compositional XEDS-SEM mapping for the **TiNbMn60h** alloy after 60 h of milling time.

Figure 8. a) Characteristic differential scanning calorimetry (DSC) results obtained for the **TiNbMn60h** alloy after 60 h of milling. b) Comparison between the characteristic XRDs before and after DSC for the same **TiNbMn60h** alloy. (O) *bcc*-TiNbMn alloy (Im3m Space Group Symmetry, SGS); (★) *fcc*-TiNbMn alloy (Fm3m SGS); (◆) *bcc*-Fe (Im3m SGS).

Figure 9. Transmission electron microscopy (TEM) bright field images and selected area electron diffraction (SAED) for the TiNbMn alloy after 10 h, **TiNbMn10h** (a), and 60 h, **TiNbMn60h** (b), of milling time.

Figure 10. High-resolution transmission electron microscopy (HRTEM) images and the corresponding fast Fourier transforms for the **TiNbMn** alloy after 10 h, **TiNbMn10h** (a), and 60 h, **TiNbMn60h** (b) of milling time. Amorphous zones are marked with a black square in **TiNbMn10h** and comprise most of the area in **TiNbMn60h**. Crystalline zones are marked with white squares in **TiNbMn60h**. The crystalline domain sizes are

marked by black (*bcc*-TiNbMn) and white (*fcc*-TiNbMn) round areas. In addition, key interplanar spacings of these phases are shown.

REFERENCES

[1] C. Leyens, M. Peters, Titanium and Titanium Alloys: Fundamentals and Applications, Wiley-VCH Verlag GmbH & Co. KGaA, 2005.
[2] G. Lütjering, J.C. Williams, Titanium, Springer-Verlag Berlin Heidelberg, 2007.
[3] R.R. Boyer, An overview on the use of titanium in the aerospace industry, Mater. Sci. Eng. A-Struct. Mater. Prop. Microstruct. Process., 213 (1996) 103-114.
[4] D.H. Kim, W.T. Kim, D.H. Kim, Formation and crystallization of Al-Ni-Ti amorphous alloys, Mater. Sci. Eng. A-Struct. Mater. Prop. Microstruct. Process., 385 (2004) 44-53.
[5] L. Bolzoni, E.M. Ruiz-Navas, E. Neubauer, E. Gordo, Mechanical properties and microstructural evolution of vacuum hot-pressed titanium and Ti–6Al–7Nb alloy, Journal of the Mechanical Behavior of Biomedical Materials, 9 (2012) 91-99.
[6] W.J. Zhang, S.C. Deevi, G.L. Chen, On the origin of superior high strength of Ti-45Al-10Nb alloys, Intermetallics, 10 (2002) 403-406.
[7] X.Y. Liu, P.K. Chu, C.X. Ding, Surface modification of titanium, titanium alloys, and related materials for biomedical applications, Mater. Sci. Eng. R-Rep., 47 (2004) 49-121.
[8] M. Niinomi, Mechanical properties of biomedical titanium alloys, Materials Science and Engineering: A, 243 (1998) 231-236.
[9] Y. Torres, P. Trueba, J.J. Pavón, E. Chicardi, P. Kamm, F. García-Moreno, J.A. Rodríguez-Ortiz, Design, processing and characterization of titanium with radial graded porosity for bone implants, Materials & Design, 110 (2016) 179-187.
[10] J.Y. Rho, R.B. Ashman, C.H. Turner, Young's modulus of trabecular and cortical bone material: Ultrasonic and microtensile measurements, Journal of Biomechanics, 26 (1993) 111-119.
[11] D.R. Sumner, Long-term implant fixation and stress-shielding in total hip replacement, Journal of Biomechanics, 48 (2015) 797-800.
[12] M. Geetha, A.K. Singh, R. Asokamani, A.K. Gogia, Ti based biomaterials, the ultimate choice for orthopaedic implants - A review, Prog. Mater. Sci., 54 (2009) 397-425.
[13] V.S.A. Challa, S. Mali, R.D.K. Misra, Reduced toxicity and superior cellular response of preosteoblasts to Ti-6Al-7Nb alloy and comparison with Ti-6Al-4V, J. Biomed. Mater. Res. Part A, 101 (2013) 2083-2089.
[14] H.C. Lin, P.H. Tsai, J.H. Ke, J.B. Li, J.S.C. Jang, C.H. Huang, J.C. Haung, Designing a toxic-element-free Ti-based amorphous alloy with remarkable supercooled liquid region for biomedical application, Intermetallics, 55 (2014) 22-27.
[15] A. Biesiekierski, J. Wang, M.A.H. Gepreel, C. Wen, A new look at biomedical Ti-based shape memory alloys, Acta Biomater., 8 (2012) 1661-1669.
[16] D. Kuroda, M. Niinomi, M. Morinaga, Y. Kato, T. Yashiro, Design and mechanical properties of new beta type titanium alloys for implant materials, Mater. Sci. Eng. A-Struct. Mater. Prop. Microstruct. Process., 243 (1998) 244-249.
[17] T. Ozaki, H. Matsumoto, S. Watanabe, S. Hanada, Beta Ti alloys with low Young's modulus, Mater. Trans., 45 (2004) 2776-2779.
[18] Q. Chen, G. Thouas, Biomaterials: A Basic Introduction, CRC Press, 2014.
[19] J.J. Pavon, P. Trueba, J.A. Rodriguez-Ortiz, Y. Torres, Development of new titanium implants with longitudinal gradient porosity by space-holder technique, Journal of Materials Science, 50 (2015) 6103-6112.

[20] Y. Torres, P. Trueba, J. Pavon, I. Montealegre, J.A. Rodriguez-Ortiz, Designing, processing and characterisation of titanium cylinders with graded porosity: An alternative to stress-shielding solutions, Materials & Design, 63 (2014) 316-324.
[21] A. Inoue, Bulk Amorphous Alloys, in: A. Inoue, K. Hashimoto (Eds.) Amorphous and Nanocrystalline Materials: Preparation, Properties, and Applications, Springer Berlin Heidelberg, Berlin, Heidelberg, 2001, pp. 1-51.
[22] A. Inoue, Chapter 14 Bulk amorphous alloys, in: C. Suryanarayana (Ed.) Pergamon Materials Series, Pergamon, 1999, pp. 375-415.
[23] M. Calin, A. Gebert, A.C. Ghinea, P.F. Gostin, S. Abdi, C. Mickel, J. Eckert, Designing biocompatible Ti-based metallic glasses for implant applications, Mater. Sci. Eng. C-Mater. Biol. Appl., 33 (2013) 875-883.
[24] T.T. Tsong, Design and characterization of materials on the atomic scale, Mater. Sci. Eng. A-Struct. Mater. Prop. Microstruct. Process., 286 (2000) 87-90.
[25] M. Schanzer, H. Mehrer, Amorphization of Nb-TM systems by mechanical alloying of the pure metals, Journal De Physique, 51 (1990) C487-C493.
[26] J.H. Li, Y. Dai, Y.Y. Cui, B.X. Liu, Atomistic theory for predicting the binary metallic glass formation, Mater. Sci. Eng. R-Rep., 72 (2011) 1-28.
[27] H. Zhang, B.W. Zhang, Prediction of binary transition transition-metal amorphous-alloys by mechanical alloying, Physica B, 205 (1995) 263-268.
[28] N. Al-Aqeeli, C. Suryanarayana, M.A. Hussein, Formation of an amorphous phase and its crystallization in the immiscible Nb-Zr system by mechanical alloying, J. Appl. Phys., 114 (2013) 153512.
[29] W.B. Pearson, Chapter VII - tabulated lattice spacings and data of the elements, A Handbook of Lattice Spacings and Structures of Metals and Alloys, Pergamon, 1958, pp. 123-130.
[30] S. Brown, Bone Nutrition, Scientific Evidence for Musculoskeletal, Bariatric, and Sports Nutrition, CRC Press, 2006, pp. 443-473.
[31] A. Nouri, P.D. Hodgson, C.E. Wen, Effect of process control agent on the porous structure and mechanical properties of a biomedical Ti-Sn-Nb alloy produced by powder metallurgy, Acta Biomater., 6 (2010) 1630-1639.
[32] A. Nouri, X.B. Chen, Y.C. Li, Y.S. Yamada, P.D. Hodgson, C.E. Wen, Synthesis of Ti-Sn-Nb alloy by powder metallurgy, Mater. Sci. Eng. A-Struct. Mater. Prop. Microstruct. Process., 485 (2008) 562-570.
[33] C. Suryanarayana, Mechanical alloying and milling, Prog. Mater. Sci., 46 (2001) 1-184.
[34] K. Tomolya, D. Janovszky, A. Sycheva, M. Sveda, T. Ferenczi, A. Roosz, Peculiarities of ball-milling induced crystalline-amorphous transformation in Cu-Zr-Al-Ni-Ti alloys, Intermetallics, 65 (2015) 117-121.
[35] N.V.Y. Scarlett, I.C. Madsen, Quantification of phases with partial or no known crystal structures, Powder Diffr., 21 (2006) 278-284.
[36] A.A. Nazarov, A.E. Romanov, R.Z. Valiev, Random disclination ensembles in ultrafine-grained materials produced by severe plastic deformation, Scripta Materialia, 34 (1996) 729-734.
[37] C.C. Koch, Materials Synthesis by mechanical alloying, Annu. Rev. Mater. Sci., 19 (1989) 121-143.
[38] X. Sauvage, G. Wilde, S.V. Divinski, Z. Horita, R.Z. Valiev, Grain boundaries in ultrafine grained materials processed by severe plastic deformation and related phenomena, Materials Science and Engineering: A, 540 (2012) 1-12.

[39] C. Aguilar, P. Guzman, S. Lascano, C. Parra, L. Bejar, A. Medina, D. Guzman, Solid solution and amorphous phase in Ti-Nb-Ta-Mn systems synthesized by mechanical alloying, Journal of Alloys and Compounds, 670 (2016) 346-355.
[40] Z.A. Munir, U. Anselmi-Tamburini, M. Ohyanagi, The effect of electric field and pressure on the synthesis and consolidation of materials: A review of the spark plasma sintering method, J. Mater. Sci., 41 (2006) 763-777.
[41] J.M. Montes, J.A. Rodriguez, F.G. Cuevas, J. Cintas, Consolidation by electrical resistance sintering of Ti powder, J. Mater. Sci., 46 (2011) 5197-5207.
[42] A. Fais, Processing characteristics and parameters in capacitor discharge sintering, J. Mater. Process. Technol., 210 (2010) 2223-2230.
[43] P.P. Chattopadhyay, S.K. Pabi, I. Manna, A metastable allotropic transformation in Nb induced by planetary ball milling, Materials Science and Engineering: A, 304 (2001) 424-428.
[44] A.H. Committees, ASM handbook. Volume 3. Alloy Phase Diagrams, ASM International, Materials Park, Ohio, 2016.
[45] S.R. Yu, X.P. Zhang, Z.M. He, Y.H. Liu, Z.H. Liu, Effects of Ce on the short-term biocompatibility of Ti-Fe-Mo-Mn-Nb-Zr alloy for dental materials, J. Mater. Sci.-Mater. Med., 15 (2004) 687-691.
[46] D. Kuroda, H. Kawasaki, S. Hiromoto, T. Hanawa, Development of new Ti-Fe-Ta and Ti-Fe-Ta-Zr system alloys for biomedical applications, Materials Transactions, 46 (2005) 1532-1539.
[47] M. Niinomi, M. Nakai, M. Hendrickson, P. Nandwana, T. Alam, D. Choudhuri, R. Banerjee, Influence of oxygen on omega phase stability in the Ti-29Nb-13Ta-4.6Zr alloy, Scripta Materialia, 123 (2016) 144-148.
[48] C. Suryanarayana, A. Inoue, Chapter 5. Cristallyzation behaviour. Bulk Metallic Glasses, CRC Press, 2011.
[49] S.L. Zhu, X.M. Wang, A. Inoue, Glass-forming ability and mechanical properties of Ti-based bulk glassy alloys with large diameters of up to 1 cm, Intermetallics, 16 (2008) 1031-1035.

Table 1. Microstructural parameters for the **TiNbMn** alloy milled for different time periods ranging from 1 h to 120 h. D: Crystalline domain size; e: Microstrain.

Specimen	**Milling time (h)**	**Lattice parameters (Å)**	**D (nm)**	**e · 10^4 (%)**	**Amorphous phase (wt. %)**
TiNbMn1h*	1	Ti: a=2.953 ± 0.010 c= 4.669 ± 0.010	Ti: 54	Ti: 21	0
		Nb: a= 3.298 ± 0.003	Nb: 43	Nb: 34	0
TiNbMn10h	10	(*bcc*) 3.374 ± 0.020	30	36.3	7.6
		(*fcc*) 4.323 ± 0.014	16.5	89	
TiNbMn20h	20	4.321 ± 0.012	6.6	53	12.8
TiNbMn40h	40	4.320 ± 0.012	6.3	19	46.3
TiNbMn60h	60	4.320 ± 0.009	5.9	3.3	51.7
TiNbMn80h	80	4.325 ± 0.015	5.7	1.8	53.7
TiNbMn100h	100	4.323 ± 0.006	5.4	6.8	50.6
TiNbMn120h	120	4.322 ± 0.006	4.8	17	47.2

Lattice parameters for raw materials:

hcp-Ti: a = 2.951 Å, c = 4.683 Å; *bcc*-Nb: a = 3.303 Å; *bcc*-Mn: a = 8.912 Å

* The values for Mn could not be determined due to the absence of high intensity peaks.

Table 2. Semiquantitative punctual XEDS composition (at.%) for the **TiNbMn** alloy, milled from 1 h to 120 h. In addition, the Fe (at. %) contamination from the milling media is shown.

Specimen	Ti	Nb	Mn	Fe
TiNbMn1	73.7 ± 5.3	20.4 ± 8.6	4.4 ± 2.6	1.4 ± 0.4
TiNbMn10	61.5 ± 1.7	31.6 ± 3.5	4.1 ± 0.6	2.8 ± 0.8
TiNbMn20	56.3 ± 3.4	29.5 ± 3.8	4.2 ± 0.2	10.0 ± 2.5
TiNbMn40	55.9 ± 1.2	28.3 ± 2.5	4.1 ± 0.3	11.7 ± 3.6
TiNbMn60	55.1 ± 1.8	27.2 ± 2.1	4.0 ± 0.4	13.7 ± 3.7
TiNbMn80	53.5 ± 3.6	26.3 ± 3.3	3.9 ± 0.5	16.2 ± 3.2
TiNbMn100	52.2 ± 2.4	24.7 ± 2.5	3.7 ± 0.3	19.4 ± 2.6
TiNbMn120	49.0 ± 2.6	23.9 ± 1.8	3.5 ± 0.8	23.6 ± 3.2

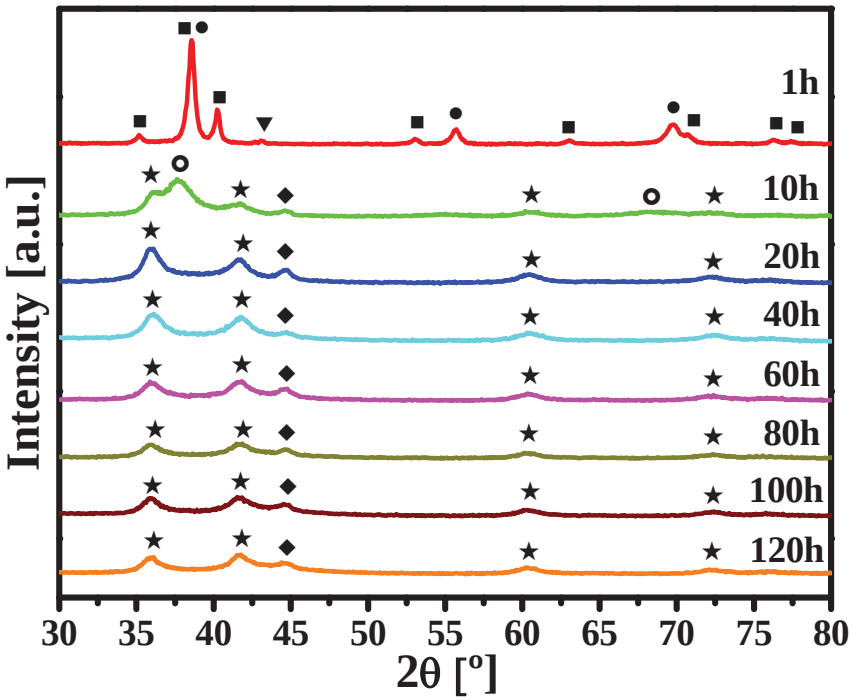
1h
10h
20h
40h
60h
80h
100h
120h
Intensity [a.u.]
30
35
40
45
50
55
60
65
70
75
80
2θ [º]

Figure 1

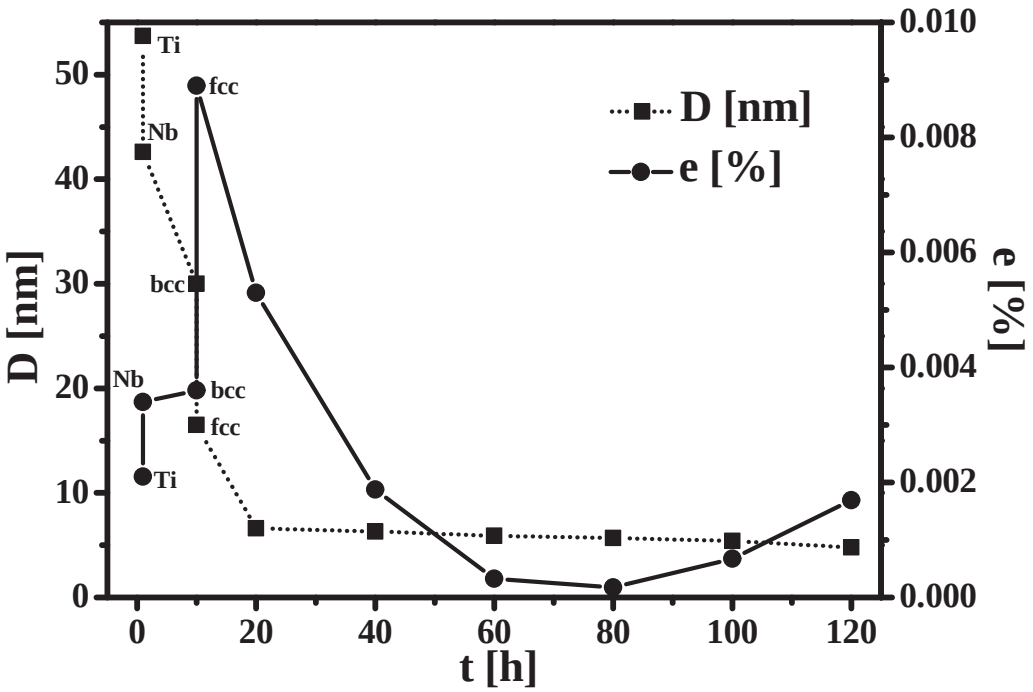
D [nm]
e [%]
Ti
fcc
Nb
bcc
Nb
bcc
fcc
Ti
D [nm]
e [%]
t [h]
0
10
20
30
40
50
0.000
0.002
0.004
0.006
0.008
0.010
0
20
40
60
80
100
120

Figure 2

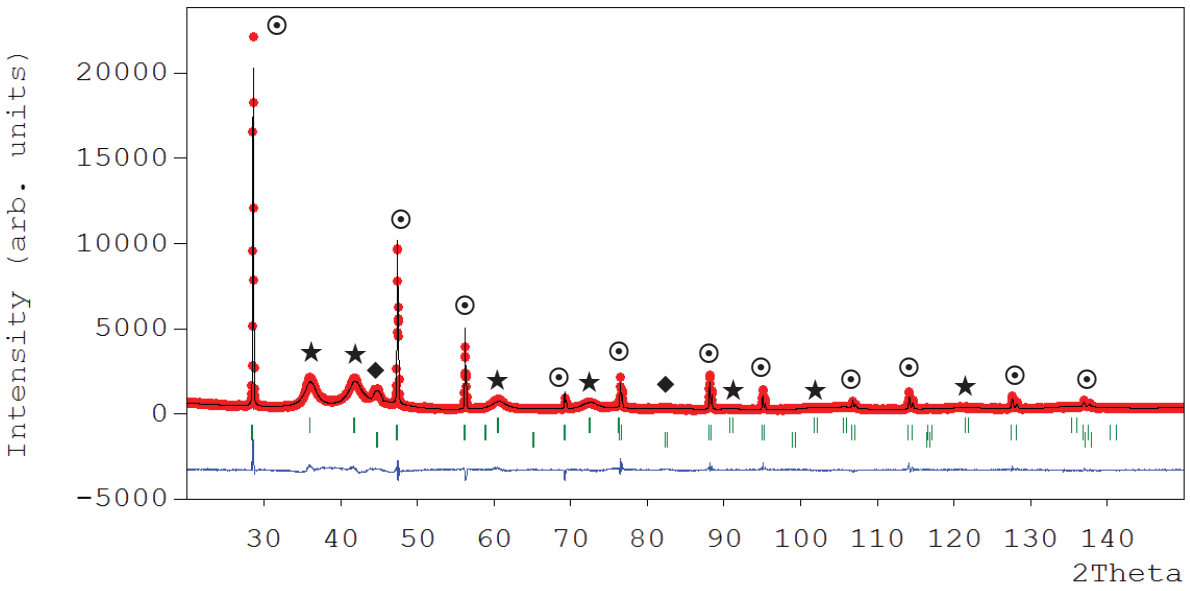
Intensity (arb. units)
20000
15000
10000
5000
0
-5000
30
40
50
60
70
80
90
100
110
120
130
140
2Theta

Figure 3

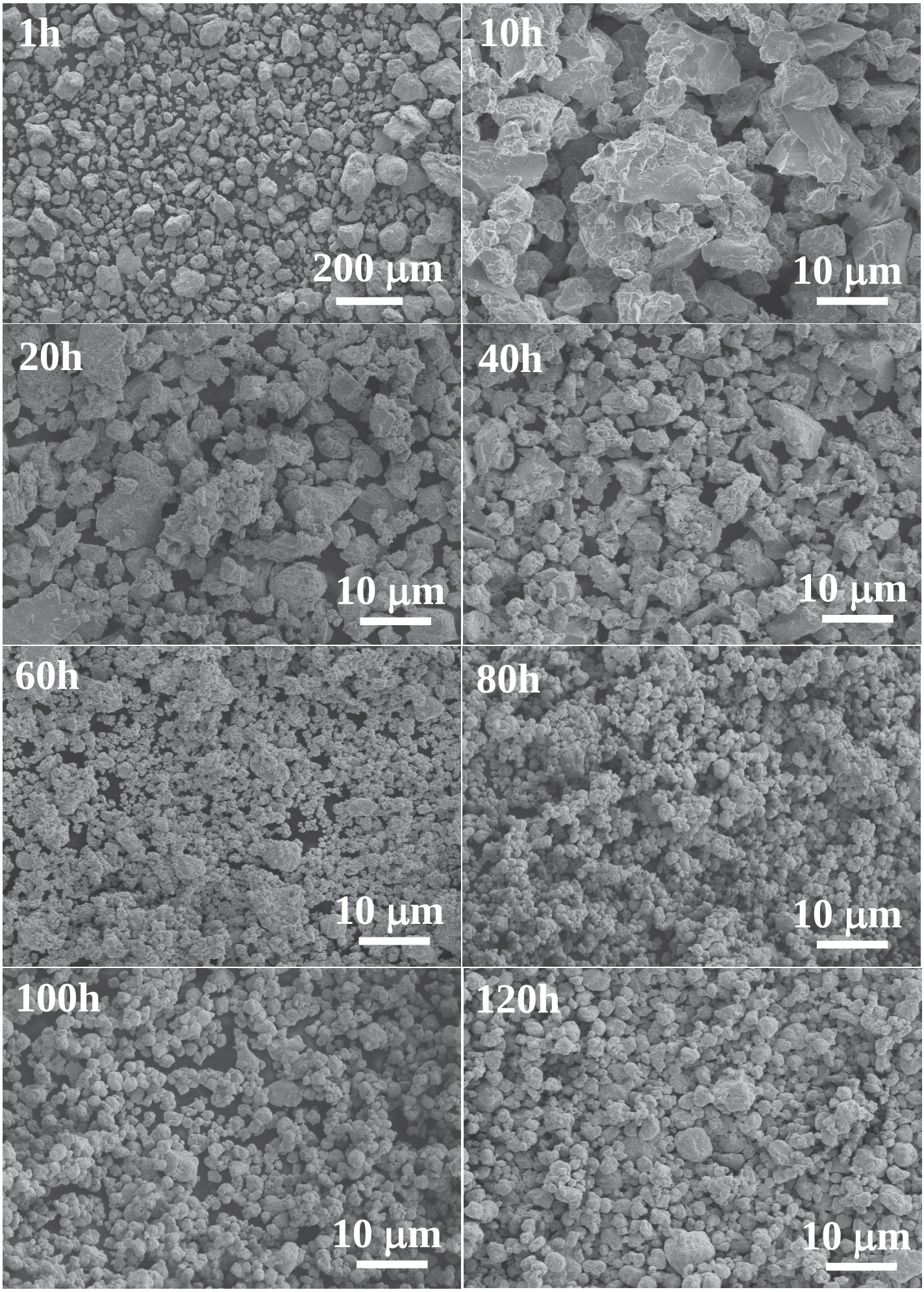
1h
200 μm
10h
10 μm
20h
10 μm
40h
10 μm
60h
10 μm
80h
10 μm
100h
10 μm
120h
10 μm

Figure 4

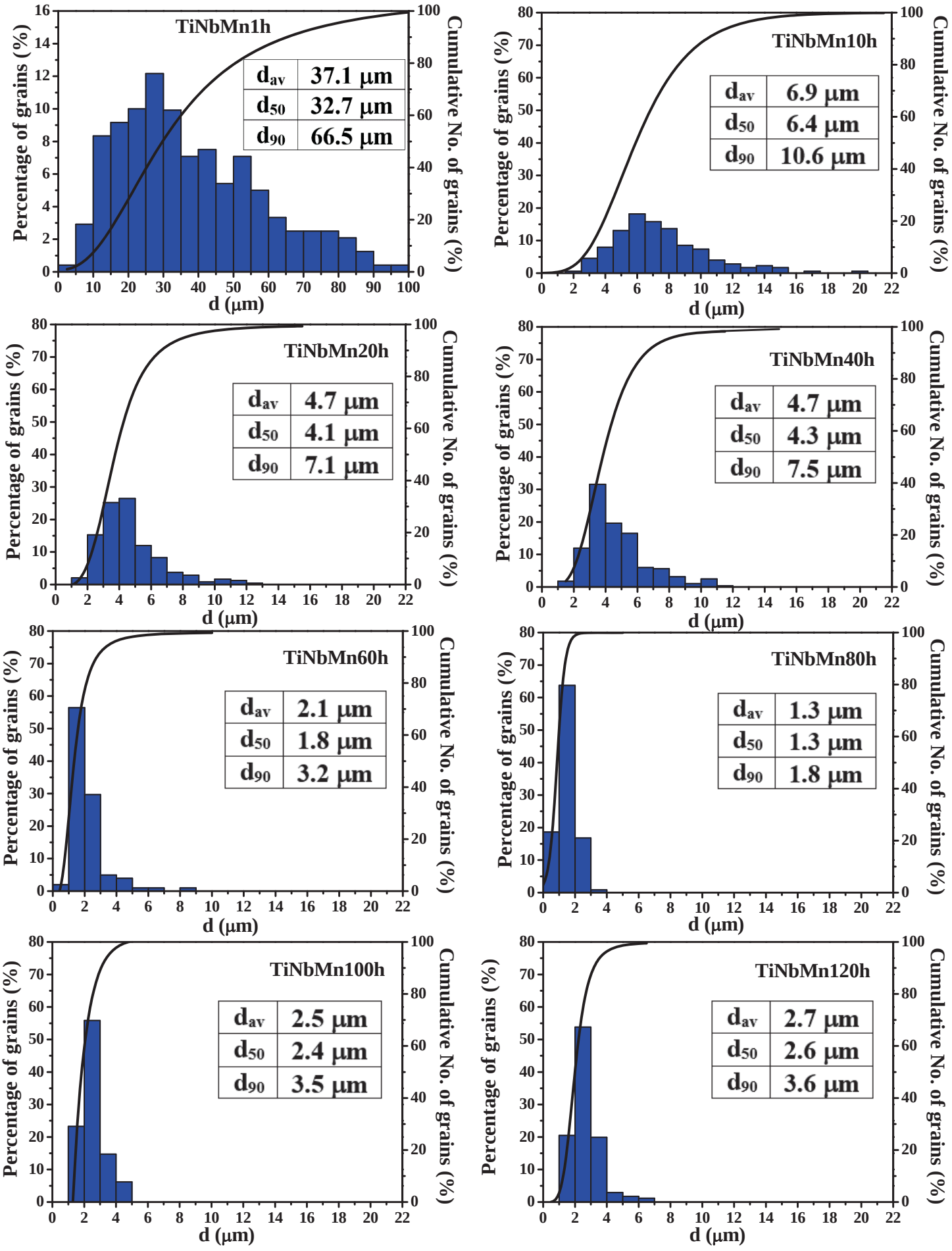
TiNbMn1h
d_{av} 37.1 μm
d_{50} 32.7 μm
d_{90} 66.5 μm
TiNbMn10h
d_{av} 6.9 μm
d_{50} 6.4 μm
d_{90} 10.6 μm
TiNbMn20h
d_{av} 4.7 μm
d_{50} 4.1 μm
d_{90} 7.1 μm
TiNbMn40h
d_{av} 4.7 μm
d_{50} 4.3 μm
d_{90} 7.5 μm
TiNbMn60h
d_{av} 2.1 μm
d_{50} 1.8 μm
d_{90} 3.2 μm
TiNbMn80h
d_{av} 1.3 μm
d_{50} 1.3 μm
d_{90} 1.8 μm
TiNbMn100h
d_{av} 2.5 μm
d_{50} 2.4 μm
d_{90} 3.5 μm
TiNbMn120h
d_{av} 2.7 μm
d_{50} 2.6 μm
d_{90} 3.6 μm
Percentage of grains (%)
Cumulative No. of grains (%)
d (μm)

Figure 5

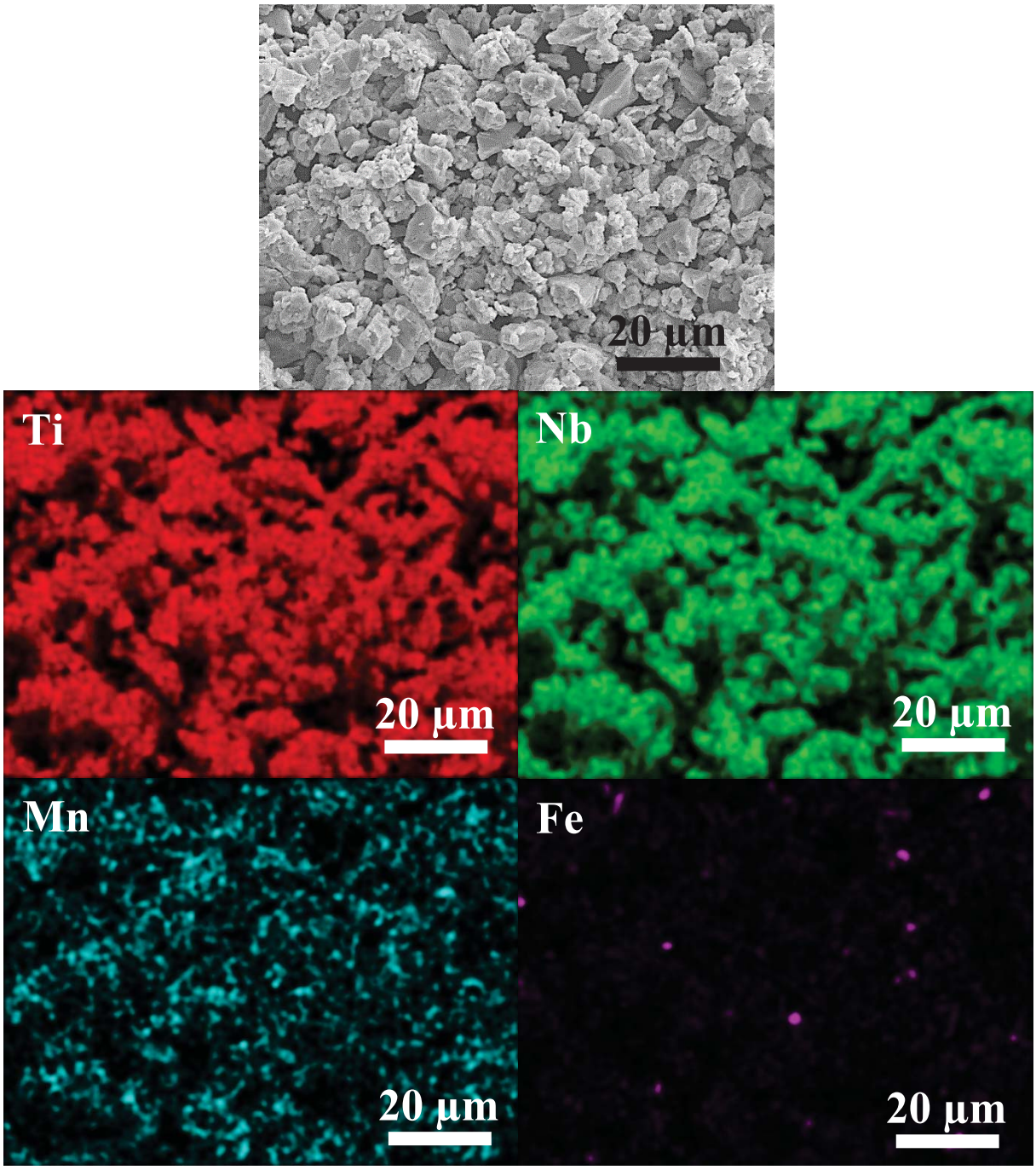

Figure 6

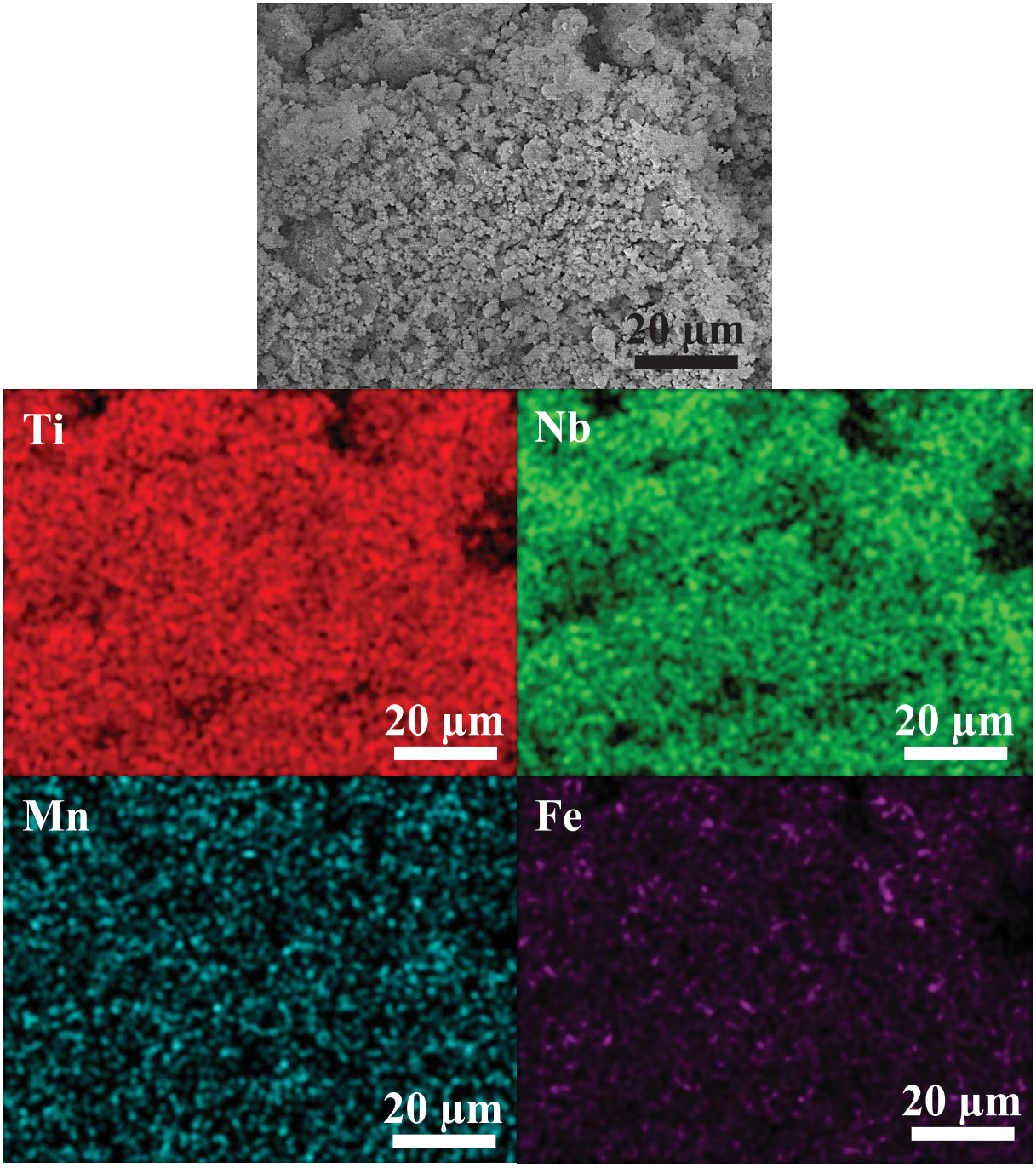

Figure 7

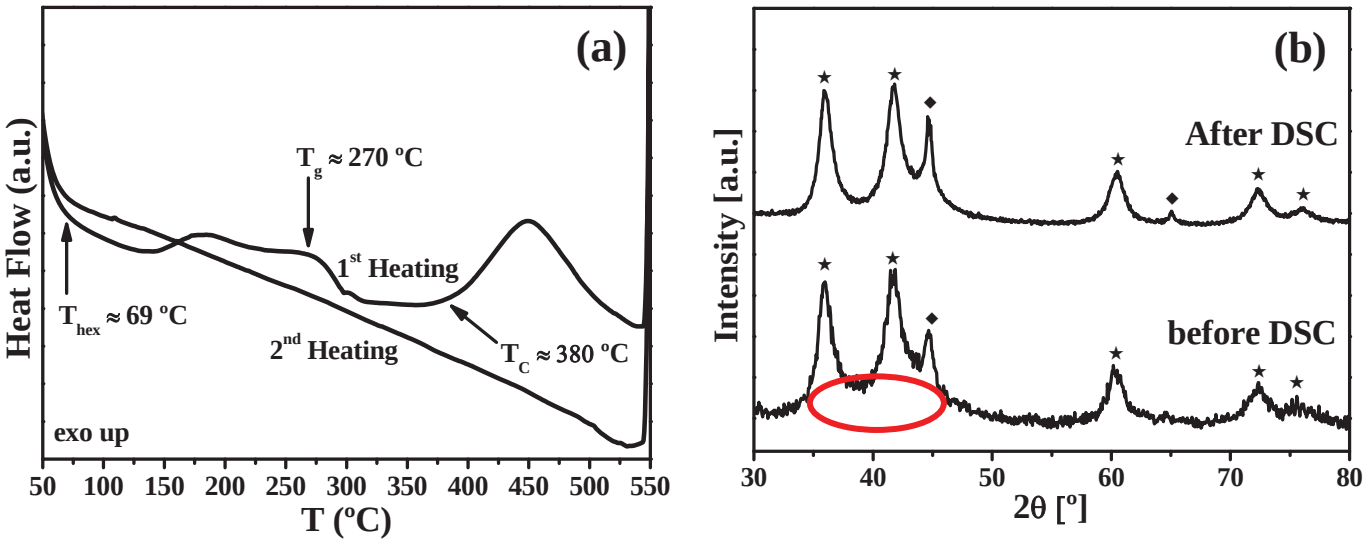
(a)
Heat Flow (a.u.)
T_g ≈ 270 °C
1st Heating
T_hex ≈ 69 °C
2nd Heating
T_C ≈ 380 °C
exo up
50 100 150 200 250 300 350 400 450 500 550
T (°C)
(b)
Intensity [a.u.]
After DSC
before DSC
30 40 50 60 70 80
2θ [°]

Figure 8

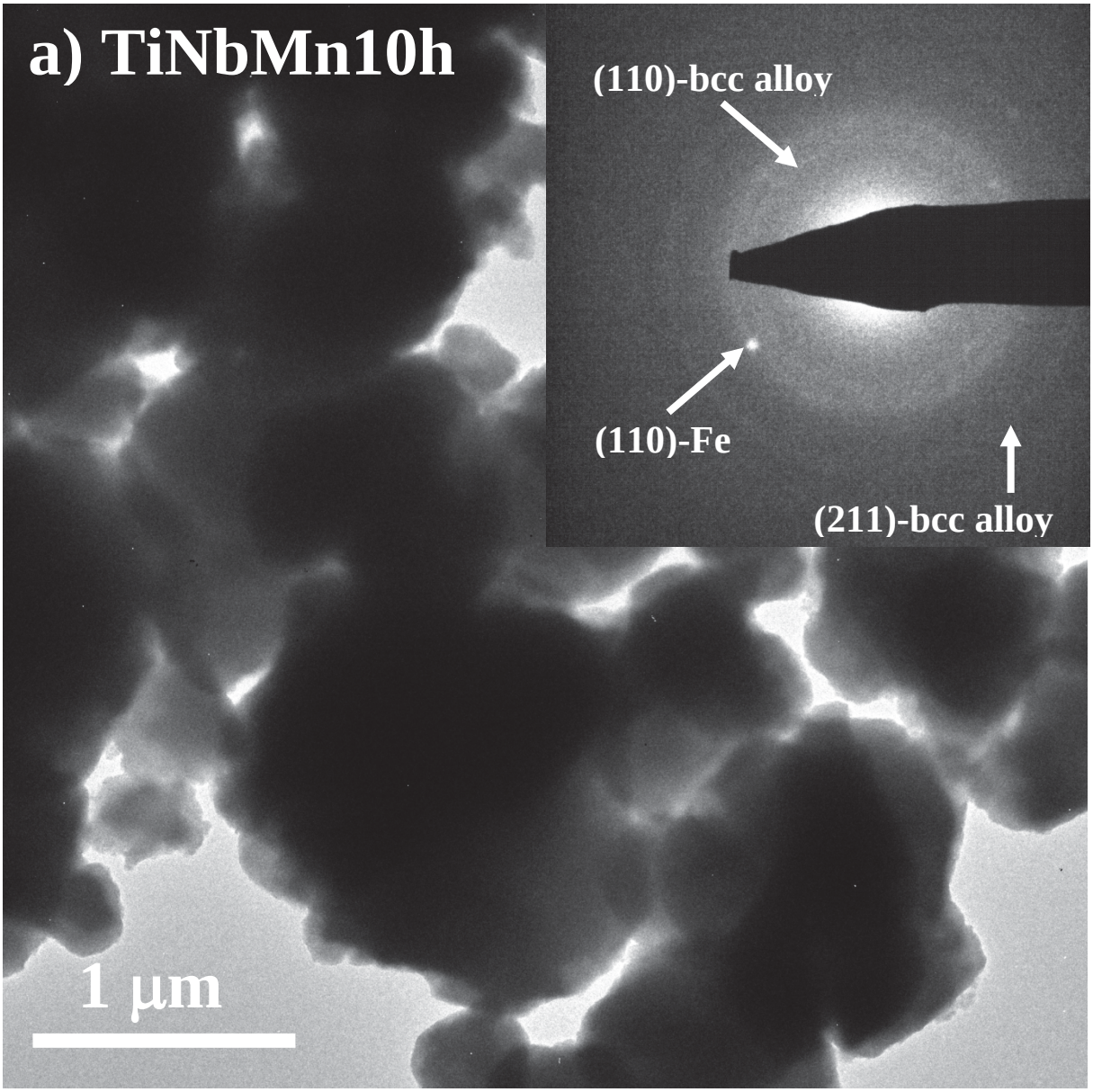
a) TiNbMn10h
(110)-bcc alloy
(110)-Fe
(211)-bcc alloy
1 μm

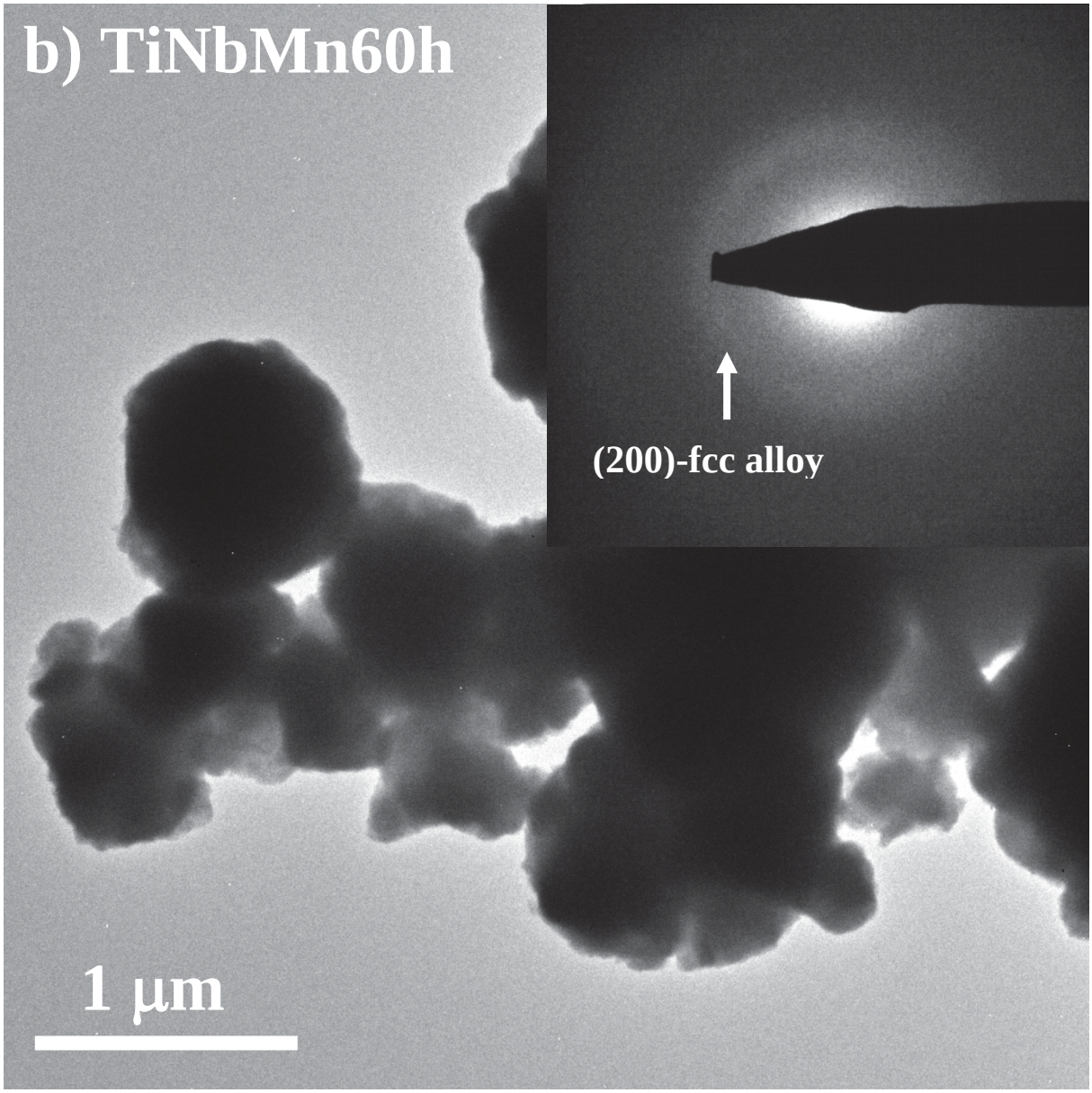

Figure 9

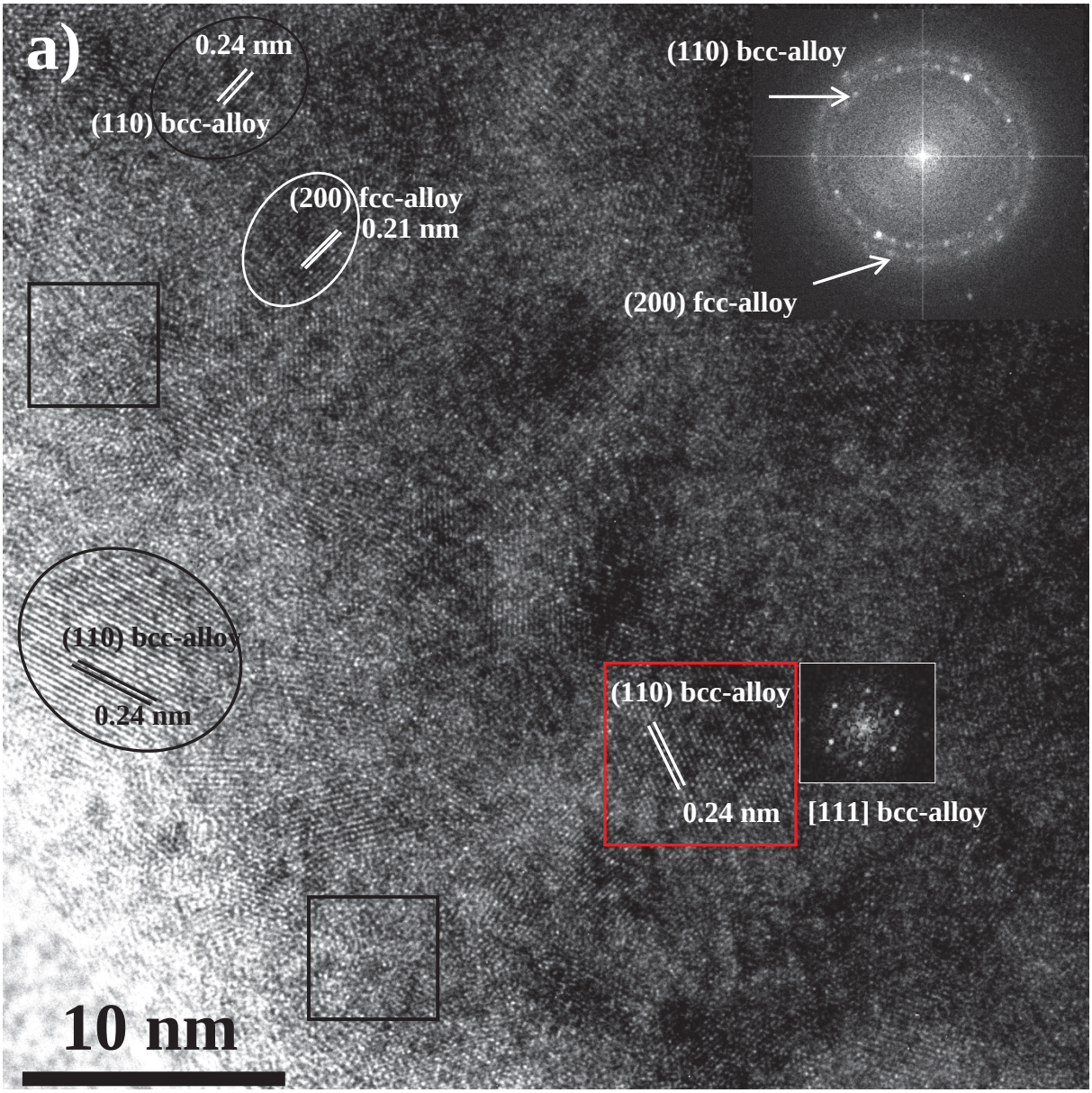
a)
0.24 nm
(110) bcc-alloy
(200) fcc-alloy
0.21 nm
(110) bcc-alloy
(200) fcc-alloy
(110) bcc-alloy
0.24 nm
(110) bcc-alloy
0.24 nm
[111] bcc-alloy
10 nm

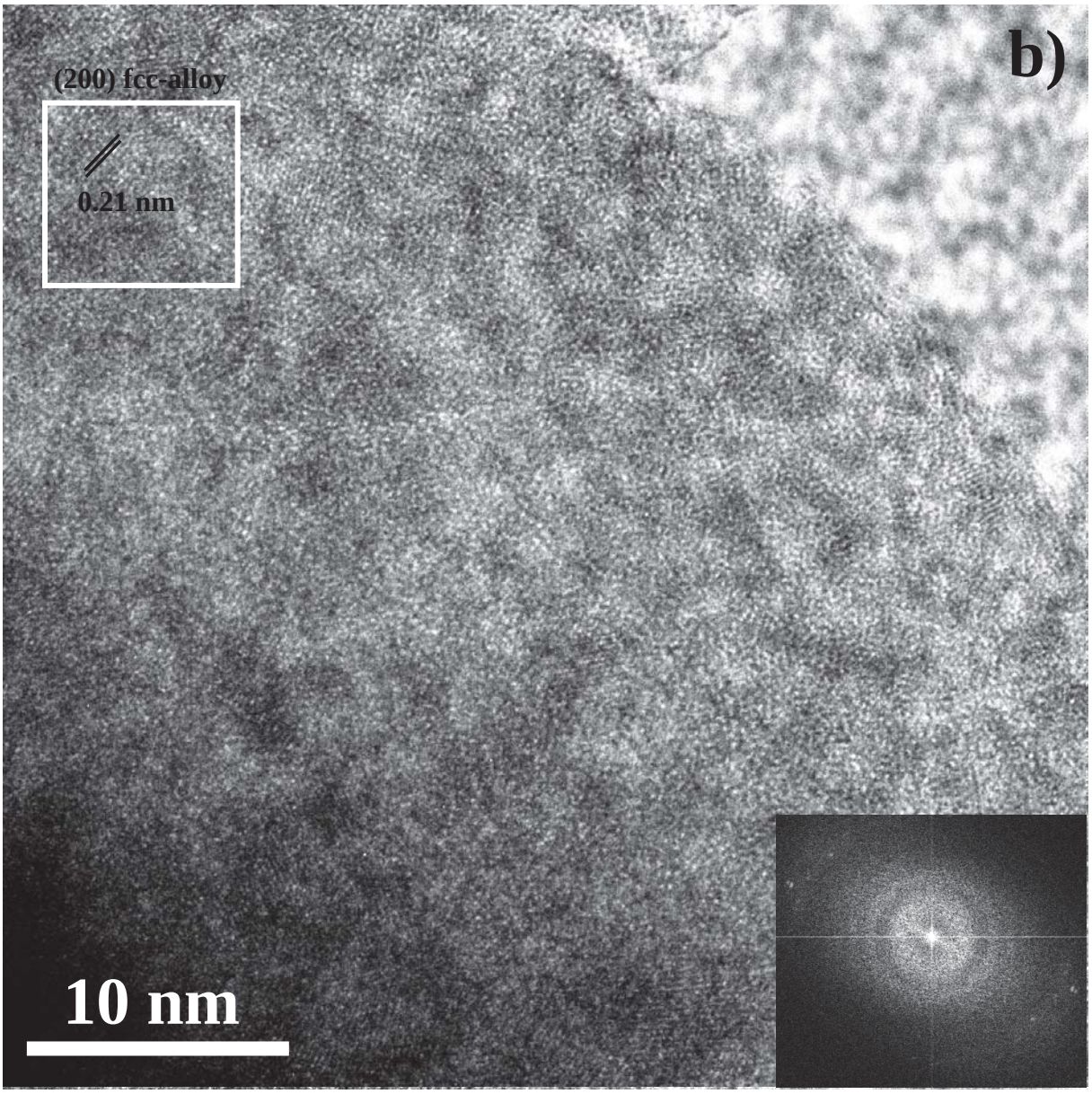

Figure 10